Biomech Model Mechanobiol (2013) 12:801–813
DOI 10.1007/s10237-012-0444-1

ORIGINAL PAPER

Helical flows and asymmetry of blood jet in dilated ascending aorta with normally functioning bicuspid valve

Elena Faggiano · Luca Antiga · Giovanni Puppini · Alfio Quarteroni · Giovanni Battista Luciani · Christian Vergara

Received: 17 April 2012 / Accepted: 20 September 2012 / Published online: 5 October 2012

Abstract Bicuspid aortic valve (BAV) is associated with aortic dilatation and aneurysm. Several studies evidenced an eccentric systolic flow in ascending aorta associated with increased wall shear stresses (WSS) and the occurrence of an helical systolic flow. This study seeks to elucidate the connections between jet asymmetry and helical flow in patients with normally functioning BAV and dilated ascending aorta. We performed a computational parametric study by varying, for a patient-specific geometry, the valve area and the flow rate entering the aorta and drawing also a tricuspid valve (TAV). We considered also phase-contrast magnetic resonance imaging of four BAV and TAV patients. Measurement of normalized flow asymmetry index, systolic WSS and of a new index (positive helix fraction, PHF) quantifying the presence of a single a single helical flow were performed. In our computation, BAV cases featured higher values of all indices with respect to TAV in both numerical and imaged-based results. Moreover, all indices increased with decreasing valve area and/or with increasing flow rate. This allowed to separate the BAV and TAV cases with respect to the jet asymmetry, WSS localization and helical flow. Interestingly, these results were obtained without modeling the leaflets.

Keywords CFD · Medical image processing · PC-MRI · BAV · Blood flow · Ascending aortic aneurysm

E. Faggiano (✉) · A. Quarteroni
MOX, Dipartimento di Matematica "F. Brioschi", Politecnico di Milano, Piazza Leonardo da Vinci 32, 20133 Milano, Italy
e-mail: elena.faggiano@mail.polimi.it

L. Antiga
OROBIX srl, Bergamo, Italy

G. Puppini
Department of Radiology, Azienda Ospedaliera Universitaria Integrata di Verona, Polo Confortini, Verona, Italy

A. Quarteroni
SB MATHICSE CMCS, EPFL, Lausanne, Switzerland

G. B. Luciani
Division of Cardiac Surgery, University of Verona, Verona, Italy

C. Vergara
Dipartimento di Ingegneria, Università di Bergamo, Bergamo, Italy

1 Introduction

Bicuspid aortic valve (BAV), the most common congenital heart disease, is related to an increased prevalence of ascending aortic dilatation and aneurysm in normally functioning valvular regime when compared to tricuspid aortic valve (TAV) (Bauer et al. 2006; Hahn et al. 1992; Nkomo et al. 2003). It is estimated that approximately 40-60 % of all BAV patients present or will present with aortic dilatation (Sievers and Sievers 2011). Furthermore, the progression of aortic dilatation in patients with normally functioning BAV usually occurs in the first two or three decades of life, but it may be observed already in school-age children (Beroukhim et al. 2006). The pathogenesis of aortic dilatation in patients with BAV remains by and large elusive. Besides the dominant hypothesis postulating a genetic origin for these vascular complications, in recent years, a complementary (rather than alternative) functional hypothesis has received an increasing attention: it states that the abnormal hemodynamics observed in patients with BAV could predispose to an enlargement of the ascending aorta and, possibly, to aneurysm formation (Barker and Markl 2011; Girdauskas et al. 2011).

In particular, it has been established that eccentric flow jets occur in the ascending aorta of normally functioning BAV patients. Figure 1 neatly shows the eccentricity of the flow at the mid-ascending aorta due to the deflection of the blood

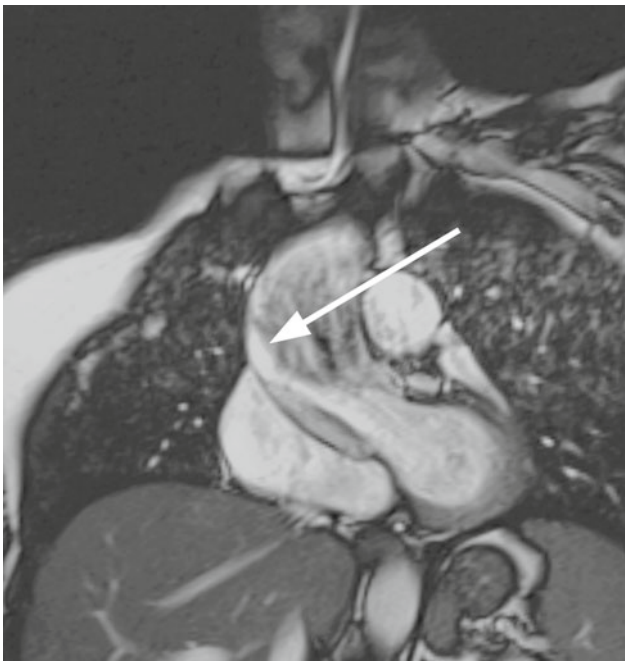

Fig. 1 An oblique magnetic resonance image of an aortic arch in a BAV patient. *Arrow* indicates the blood flow deflection toward the aortic wall

jet which, instead of proceeding along the central axis of the aorta, it deviates toward the wall.Eccentric flow in BAV has been reported by several techniques, in particular echocardiographic evaluations (Fowles et al. 1979), phase-contrast magnetic resonance imaging (PC-MRI) (Barker et al. 2012; Hope et al. 2010; Sigovan et al. 2011; Den Reijer et al. 2010) and computational methods (Chandra et al. 2012; Della Corte et al. 2011; Vergara et al. 2011; Viscardi et al. 2010). This asymmetry was found to be strictly related to increased wall viscous stresses exerted by the blood on the lumen surface, as highlighted by PC-MRI techniques (Barker et al. 2010, 2012; Hope et al. 2011), and by computational models (Viscardi et al. 2010; Vergara et al. 2011). Wall blood stresses are supposed to play an important role in vascular remodeling and in aneurysm formation. Indeed, an increased hemodynamic load placed on the proximal aorta could possibly result in progressive aortic dilatation (Della Corte et al. 2008).

On the basis of these observations, the causes of formation and development of eccentric flows have to be investigated in order to deeply understand the phenomenon of the dilatation of the ascending aorta in patients with normally functioning BAV. In this respect, an interesting observation is that blood flow jet asymmetry is also found in BAV patients featuring normal aortic dimensions (Hope et al. 2010). This leads to formulating the conjecture that blood jet asymmetry may be due to the interplay between morphology and hemodynamics in BAV configurations, and it precedes aorta dilatation. However, in dilated aortas, it has been observed that the jet eccentricity increases. In particular, in Den Reijer et al. (2010), the authors found a significant correlation between the blood flow jet angle and the diameter at different levels of the ascending aorta.

Another phenomenon characterizing the abnormal fluid-dynamics in a BAV ascending aorta is the helical systolic flow (Hope et al. 2010; Barker et al. 2012). In a normal TAV subject, retrograde/helical flows develop just at diastole, while in patients with ascending aortic aneurysm, they originate at systole, together with a skewed peak velocity (Hope et al. 2007). In patients with normally functioning BAV, systolic helical flow can appear in a normal ascending aorta, becoming particularly intense in dilated or aneurysmatic cases, as observed with PC-MRI (Hope et al. 2010).

In this paper, we focus on the study of blood jet asymmetry in BAV patients with a dilated aorta but with non-stenotic aortic valve orifice. Our aim is to understand more deeply the phenomenon observed in Den Reijer et al. (2010). In particular, we try to relate this phenomenon to the systolic helical flow observed with PC-MRI. With this goal, we consider the real geometry of one dilated BAV patient, and we perform a computational parametric study by varying the valve area (always in a non-stenotic range) and the flow rate entering the aorta. Besides we consider for the same dilated geometry a tricuspid valve in order to make comparisons with BAV cases. Our study is therefore performed on one fixed aorta geometry with different virtual scenarios. The computational study consists in the numerical simulation of the fluid-dynamics inside the aorta for all the different virtual scenarios, without valve leaflets and ventricular mechanics modeling. To find relations between hemodynamic phenomena, we introduce suitable indices, allowing us to monitor for each case the flow vorticity, the flow reversal and the jet deflections. Finally, to further validate the correctness of the relation between helical flow and jet asymmetry found by our numerical results, we analyze PC-MRI images of BAV and TAV patients.

2 Materials and methods

2.1 Patient dataset

A dataset was formed by four BAV patients without valve stenosis and insufficiency, and by four TAV patients. In Table 1, several demographic information and aortic diameters for BAV patients (B) and TAV patients (T) are reported. Body surface area (BSA) was calculated by Haycock's formula (Haycock et al. 1978) and was then used to normalize age and size effects in ascending aorta diameters calculation. All BAV patients had a dilated ascending aorta [ascending aorta diameter $\geq$4 cm or normalized ascending aorta diameter $\geq$2.2 cm/m^2 (Roman et al. 1989)]. Each BAV patient presented a right-left leaflets fusion. None of the patients

Table 1 Demographic information and aortic diameters for BAV (B) and TAV (T) patients

	B1	B2	B3	B4	T1	T2	T3	T4
Age (year)	39	46	38	22	21	21	24	21
Sex (M, F)	F	M	M	M	F	M	M	F
BSA (m^2)	1.7	2.2	2.5	2.0	1.4	1.8	1.9	1.8
Annulus (cm)	2.5	2.0	3.2	3.5	X	X	X	X
SV (cm)	3.4	2.7	4.8	3.6	X	X	X	X
STJ (cm)	3.7	2.4	4.4	4.1	X	X	X	X
AAo (cm)	4.0	5.0	5.0	4.1	2.5	3.1	2.7	2.6
AAo/BSA (cm/m^2)	2.4	2.3	2.0	2.0	1.8	1.7	1.4	1.4

B Bicuspid aortic valve, *T* tricuspid aortic valve, *BSA* body surface area, *SV* sinus of valsalva, *STJ* sinotubular junction, *AAo* ascending aorta, *AAo/BSA* normalized AAo size, *X* data not available

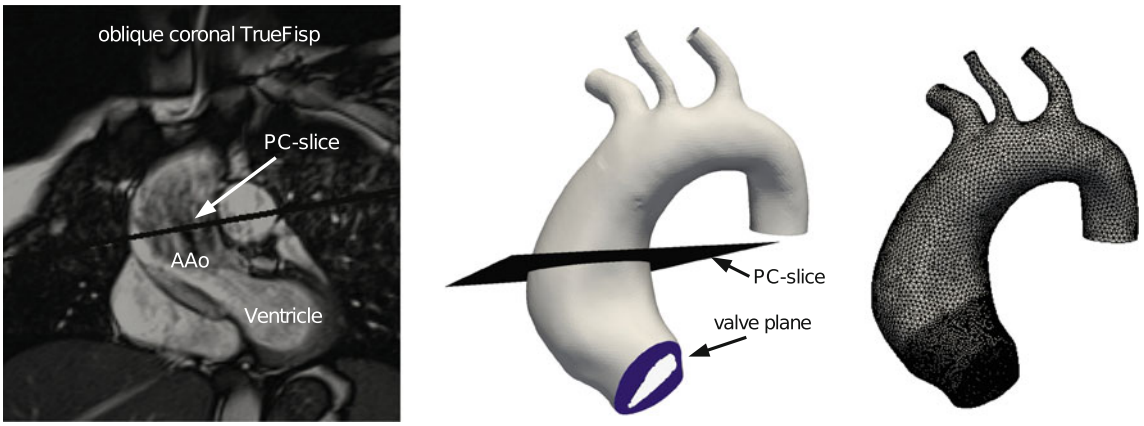

Fig. 2 *Left*: oblique coronal TrueFisp image of one patient with superimposed the PC-slice. *Middle*: aortic arch reconstruction for the selected BAV patient where the PC-slice and the valve plane are highlighted. On the valve plane, the root region is depicted in *blue* while a representative valve orifice is depicted in *white*. *Right*: solid model after the refinement step; the mesh was refined close to the root

was affected by additional structural heart disease, including aortic coarctation or tetralogy of Fallot.

For each BAV and TAV patient, a 2D CINE PC-MRI was acquired. An oblique imaging slice (PC-slice) was positioned in the mid-ascending aorta approximately at 2 cm from the most distal feature of the sinotubular junction, as can be seen in Fig. 2. Temporal resolution was 20 phases in one cardiac cycle with a pixel resolution of 1.17×1.17 mm. Velocity encoding values were chosen to optimize the velocity map resolution with values ranging from 150 to 200 cm/s. The following parameters were also used: TE (echo time) = 6.4 ms; flip angle = 15 deg; slice thickness = 5 mm; acquisition matrix = 256×256.

A breath-hold true fast imaging with steady-state precession (TrueFisp) cine-sequence with retrogated ECG triggering was also acquired on oblique coronal slice, see Fig. 2, left. For a multiphase imaging of the bicuspid aortic valve, TrueFisp images were acquired also on the valve plane. Oblique and valve TrueFisp images were performed using the following parameters: TE (Echo Time) = 1.6 ms; flip angle = 65deg; slice thickness = 8 mm; temporal resolution = 20 phases in one cardiac cycle; acquisition matrix = 256×146.

For BAV patients, a 3D contrast-enhanced MRI (CE-MRI) was acquired with a voxel resolution of $1.72 \times 1.72 \times 1.5$ mm. The following parameters were used: TE (Echo Time) = 1.02 ms; flip angle = 20deg; slice thickness = 1.5 mm; acquisition matrix = 256×106.

All the MRI acquisitions were performed on a 1.5 Tesla system (Magnetom Symphony, Siemens Medical Systems, Erlangen, Germany).

Institutional Review Board approval was obtained for the conduct of this study, and the board waived the need for patient consent.

2.2 Mesh generation

A surface model of the aortic root, ascending aorta and aortic arch of one of the four BAV patients (B1) was obtained from the 3D CE-MRI image using a level-set segmentation technique provided by the Vascular Modeling Toolkit (vmtk, http://www.vmtk.org). This technique allows the generation of a surface representing the interface between the blood and the arterial wall. The surface was then cut at the aortic valve plane with a plane corresponding to the TrueFisp valve acquisition and at the outlets by planes perpendicular to the

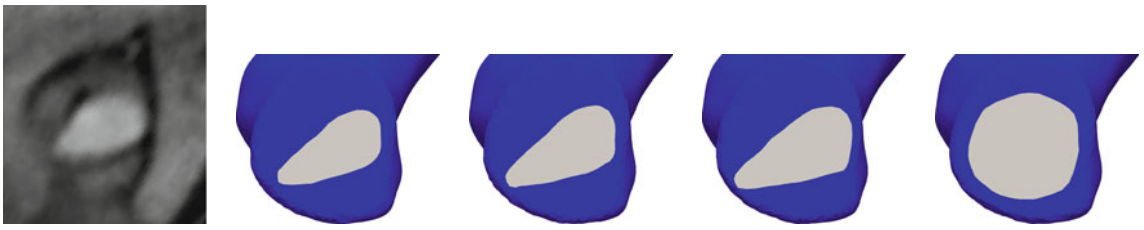

Fig. 3 TrueFisp image of the aortic valve plane of BAV patient 1 in the systolic phase (*B1*) and a zoom of the valve plane of the solid reconstructed model of the same patient with the 4 drawn valve orifices in *white* (*Bn1*, *Bn2*, *Bn3* and *Tn*)

Table 2 Values of A_{val}/A_{root} and A_{val} for B1 patient (at systole, from TrueFisp image) and for the reconstructed valve orifices (mapped onto the diastolic configuration)

	B1	Bn1	Bn2	Bn3	Tn
A_{val}/A_{root}	0.26	0.26	0.29	0.33	0.51
A_{val} (cm^2)	2.5	1.6	1.8	2.0	3.1

lumen longitudinal axis. We then manually delineated the valve orifice on the valve plane, by using a tool which allows to choose the valve shape, dimension and position. In detail, the tool implemented by us in the vmtk framework allows to visualize the TrueFisp valve image, where the aortic arch model is superimposed, and to manually draw the valve hole on the model. At the end of the procedure, two regions can be identified on the valve plane (see Fig. 2, center): the valve orifice which is the inlet for the simulations and the aortic root region which is assimilated to the aortic wall during simulations.

In this work, we were interested in describing the systolic fluid-dynamics, so that we computed by the TrueFisp image the values of the valve and root areas, A_{val} and A_{root}, at systole. Since the CE-MRI acquisition could be assimilated to the diastolic phase of the cardiac cycle, we mapped the systolic valve orifice obtained by the TrueFisp image onto this diastolic configuration (Bn1), by maintaining the value A_{val}/A_{root} constant. Moreover, in view of the parametric study, we delineated two more different bicuspid valve orifices (Bn2 and Bn3) with a shape similar to the original one, always maintaining the valve area in a non-stenotic range. A tricuspid orifice (Tn) was also delineated to simulate in the same aorta geometry the tricuspid case. In Fig. 3, the TrueFisp image at systole and the four valves (Bn1, Bn2, Bn3 and Tn) are shown. In Table 2, the values of A_{val}/A_{root} ratio and of A_{val} for patient B1 and for the four simulated cases are reported.

The obtained solid models were successively turned into volumetric meshes of linear tetrahedra (Antiga et al. 2008) using vmtk, in order for computational fluid-dynamics (CFD) simulations to be carried out (see Fig. 2, right). We observe the refined surface meshes in the area near the valve for better capturing the expected detachment and deflection of the flow.

The mesh for one numerical simulation was made of 1.36×10^6 tetrahedra. This number was chosen after a grid convergence analysis performed according to Celik et al. (2008) as reported in Appendix.

2.3 Numerical simulations

Unsteady numerical simulations were performed in the four scenarios described above, by using the finite element library LifeV (http://www.lifev.org). Blood was considered as Newtonian, homogeneous, and incompressible, so that the Navier–Stokes equations for incompressible fluids were used for the mathematical description (Formaggia et al. 2009). Blood viscosity was set equal to 0.035 Poise and the density equal to 1.0 g/cm^3. The time step was chosen equal to 0.01s. For time independency, we tested that doubling the time step the results remained the same. The vessel wall was considered rigid since we do not expect that the dynamics of the wall substantially affects the phenomena under study. Being interested in the hemodynamics at systolic ejection, valve leaflets were not modeled as we assumed that it would not influence the direction of the jet at systole, due to the higher pressure of blood exiting from the left ventricle compared to the pressure in the Valsalva sinuses. The valve was therefore formed only by the orifice and the inflow conditions were prescribed in the orifice nodes (i.e., in the nodes belonging to the white regions in Fig. 3). Valve opening and closing were therefore modeled in an on/off modality without modeling the intermediate steps. More precisely, the off modality corresponds to the valve completely closed (end diastolic phase, null velocity prescription), while the on modality corresponds to the valve completely open (the rest of the cardiac cycle, non-null flat velocity prescription). We considered the patient-specific unsteady flow rate measured by PC-MRI (Fig. 4), and we prescribed three different curves obtained by the original one multiplied by 1, 1.2 and 1.4 (Q1 = 1 × original, Q2 = 1.2 × original, Q3 = 1.4 × original), respectively, obtaining a flow rate at systole equal to 13.63,

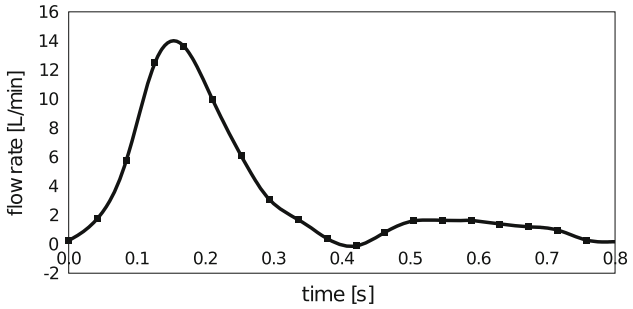

Fig. 4 Flow rate curve obtained from PC-MRI images of patient B1

16.36 and 19.09 L/min, respectively. The choice of prescribing flow rates greater than the measured one was suggested by the fact the PC-MRI often under-estimates the flow values (Baltes et al. 2008). To prescribe this flow rate, a Dirichlet boundary condition at the inflow under the assumption of flat velocity profile was imposed (Moireau et al. 2012). At the outlets, a zero-stress condition was prescribed, since the region of interest is in the proximal ascending aorta. It must be highlighted that, as pointed out in Nichols and O'Rourke (1998), in TAV cases, transitional flow is only expected to be present near the aortic valve, supposedly being absent in the ascending aorta. We assumed that this hypothesis holds also for BAV cases, so that no turbulence models were assumed (see Sect. 4, paragraph *Limitations*).

2.4 Quantitative measures

To better describe the fluid-dynamics in the ascending aorta, we introduced suitable indices to be computed starting from both the results obtained in our numerical simulations and image data.

For the latter, we processed the phase-contrast images for each BAV and TAV case to obtain a velocity vector field. We point out that the following indices were defined on a triangular grid for the numerical results, while on a pixelized grid for the in-vivo data.

Retrograde flow analysis. To quantify the retrograde flow, we measured the flow reversal ratio (FRR) at systole at the PC-slice Γ, defined as

$$\mathrm{FRR} = \frac{|Q_{\mathrm{neg}}(t_{\mathrm{sys}})|}{Q_{\mathrm{pos}}(t_{\mathrm{sys}})} \times 100,$$

where $Q_{\mathrm{neg}}(t_{\mathrm{sys}}) := \int_\Gamma \mathbf{v}^-(t_{\mathrm{sys}}) \cdot \mathbf{n}\, \mathrm{d}\sigma$ and $Q_{\mathrm{pos}}(t_{\mathrm{sys}}) := \int_\Gamma \mathbf{v}^+(t_{\mathrm{sys}}) \cdot \mathbf{n}\, \mathrm{d}\sigma$, with $\mathbf{v}^- \cdot \mathbf{n}|_\Gamma \leq 0$ and $\mathbf{v}^+ \cdot \mathbf{n}|_\Gamma > 0$, represent the backward and forward flow rates.

Flow asymmetry. To quantify flow eccentricity, we used the normalized flow asymmetry index (NFA) proposed in Sigovan et al. (2011). NFA was calculated as the euclidean distance between the center of velocity at Γ of the forward flow C_{vel} at systole, defined as

$$C_{\mathrm{vel},j} = \frac{\int_\Gamma j\mathbf{v}^+(t_{\mathrm{sys}}) \cdot \mathbf{n}\, \mathrm{d}\sigma}{\int_\Gamma \mathbf{v}^+(t_{\mathrm{sys}}) \cdot \mathbf{n}\, \mathrm{d}\sigma} \qquad j = x, y, z,$$

and the center of Γ normalized to the lumen radius. Lumen radius has been computed by mapping the lumen onto a circle. This yields a NFA index equal to 0 when the center of forward velocity is in the center of the vessel (no asymmetric flow) and equal to 1 when it is on the vessel wall (totally asymmetric flow).

Wall shear stress. We introduced a wall shear stress index, WSSRegion which is the maximum of wall shear stress evaluated on a portion of the ascending aorta (Vergara et al. 2011).

Helical flow pattern analysis. Measures of helical pattern were proposed and extensively studied by Morbiducci et al. (2010). However, these indices are applicable only knowing the complete three-dimensional velocity field and therefore cannot be used in our application. Therefore, we introduced a new quantitative index to measure the helical flow pattern knowing the velocity field only on one slice (e.g., the PC-slice). We preliminarily defined the quantity h calculated over the PC-slice as the dot product between the vorticity of the velocity parallel to the slice and the normal to the slice, $h := (\nabla \times ((\mathbf{v}(\mathbf{t}) \cdot \boldsymbol{\tau})\boldsymbol{\tau})) \cdot \mathbf{n}$, where $\boldsymbol{\tau}$ is the tangent plane to the PC-slice. h_i is then defined for each triangle (or pixel) of the slice and is positive or negative if the flow has a local right-handed or left-handed rotational structure, respectively. The positive helix fraction (PHF) at systole was then calculated as

$$\mathrm{PHF} = \frac{H_{\mathrm{pos}}}{H_{\mathrm{pos}} + H_{\mathrm{neg}}},$$

where $H_{\mathrm{pos}} = \int_\Gamma h^+(t_{\mathrm{sys}})\, \mathrm{d}\sigma$ and $H_{\mathrm{neg}} = \int_\Gamma h^-(t_{\mathrm{sys}})\, \mathrm{d}\sigma$, with $h^+ > 0$ and $h^- < 0$. PHF indicates the ratio between right-handed helix and the totality of the rotating flux (PHF = 1 means complete right-handed helical flow, PHF = 0 means complete left-handed helical flow, PHF = 0.5 means no prevalence of any direction), and was introduced to quantify the prevalence of right-handed helical flow in BAV patients. To eliminate border effects due to no-slip data, we cut with a sphere the PC-slice and calculated the PHF index only inside the extracted area.

For the computation of such indices, we developed a tool based on the Visualization Toolkit library (VTK, http://www.vtk.org).

The integrals in the formulas were calculated using mean point quadrature rule.

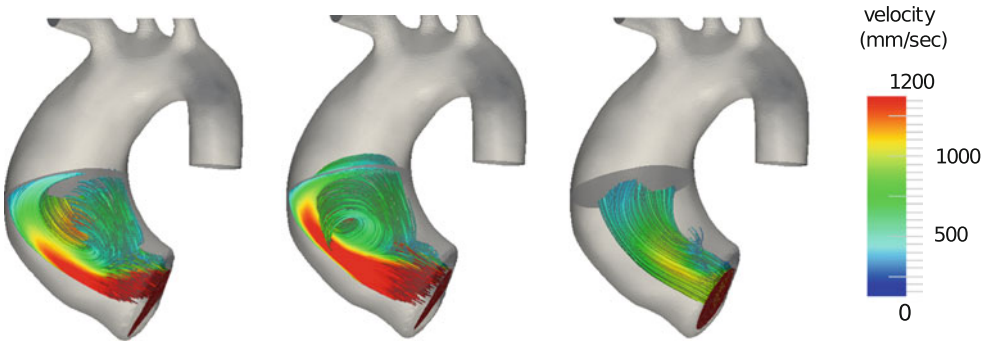

Fig. 5 Streamlines of the velocity fields in three significant cases. Q2 = 1.2 × original flow rate

3 Results

This section is divided into two parts. In the first part, we report the results of the CFD simulations for the different valve orifices described in Sect. 2.2 and the different inflow boundary conditions described in Sect. 2.3. After a first view of the overall flow pattern in the ascending aorta, we present the values obtained for the proposed indices. In the second part, we analyze the in-vivo data computing the same indices to confirm and strengthen the numerical findings.

3.1 Numerical simulations

3.1.1 Preliminary analysis

A first snapshot of the flow pattern in the ascending aorta is shown in Fig. 5. In this figure, the streamlines entering the PC-slice at systole are reported for the three significative cases: the largest bicuspid valve (Bn3), the smallest bicuspid valve (Bn1) and the tricuspid case (Tn), all of them with the mid-value inflow condition Q2.From this figure, the marked difference between the fluid-dynamics in the first tract of the ascending aorta in TAV and BAV cases could be appreciated. Indeed, in the BAV cases, we observed a recirculating vortex that forces the flow exiting from the valve to deviate toward the aortic wall. From a comparison between the two BAV cases, we preliminary observed that the more the valve is narrowed, the more the vortex is marked, making the deflection of the jet more evident (see Fig. 5, left and middle). Concerning the TAV case, we observed no recirculation zones and no deflection of the flow exiting the valve (Fig. 5, right).

3.1.2 Retrograde flow analysis

All the simulated BAV presented a retrograde flow at systole at the PC-slice. In Table 3, the values of FRR for all the simulations are reported. We observe that FRR increases by decreasing the area of the orifice or by increasing the flow rate. In all tricuspid cases, FRR is very small (more than 20 times smaller than Bn3) indicating no retrograde flow for this configuration. For the BAV cases, this index features higher values, reaching almost the value of 30 %.

Table 3 FRR index (in %) for numerical simulations

Valve/flux	Q1	Q2	Q3
Bn1	15.79	27.79	28.07
Bn2	9.20	19.35	24.06
Bn3	5.32	13.36	19.74
TRI	0.00	0.00	0.83

Q1 = 1 × original flow rate, Q2 = 1.2 × original flow rate, Q3 = 1.4 × original flow rate

3.1.3 Flow asymmetry

All simulated BAV presented an evident deflection of the flow toward the aortic wall, which was completely absent in the tricuspid case. In Fig. 6, we reported on an oblique TrueFisp slice the velocity pattern at systole obtained by numerical results in a BAV (middle) and in a TAV case (right). In the BAV case, the flow originates straight from the valve, and it then deviates toward the outer wall. A completely different situation occurs for TAV, where the flux does not deviate toward the wall but goes straight covering the shortest path to reach the mid-ascending aorta.

In Table 4, the values of the NFA index are reported for all the cases. This index features a behavior similar to that of FRR. Indeed, it seemed to be inversely proportional to the valve orifice dimension and directly proportional to the flow rate. In tricuspid cases, as expected, the NFA value was smaller, indicating an almost total absence of flow deflection.

3.1.4 Wall shear stress

In Fig. 7 left, we reported the region of interest where WSS-Region was computed, whereas, in Table 5, WSSRegion is reported for all the performed simulations.

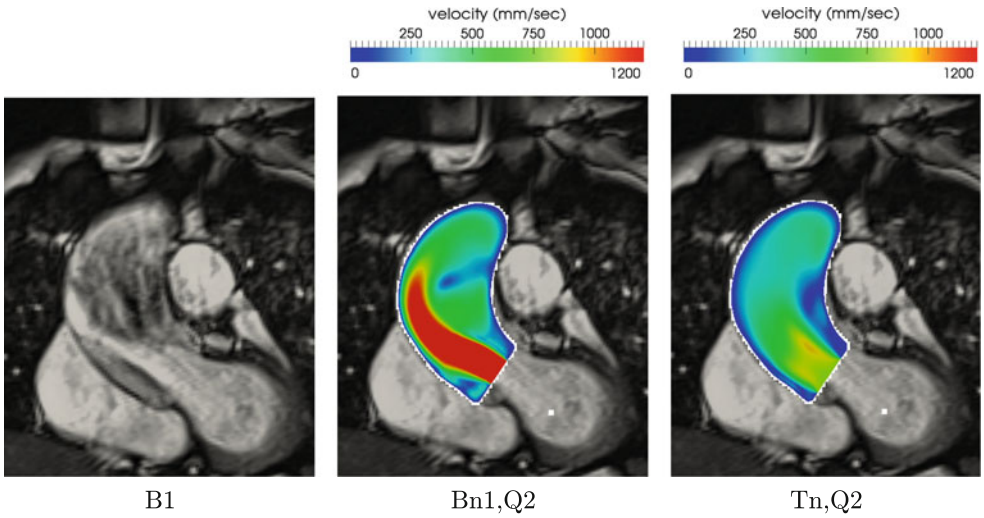

Fig. 6 Velocity patterns obtained by the numerical solutions reported on the oblique TrueFisp slice on the left. Q2 = 1.2 × original flow rate

Table 4 NFA index for numerical simulations

Valve/flux	Q1	Q2	Q3
Bn1	0.40	0.50	0.51
Bn2	0.32	0.44	0.50
Bn3	0.25	0.37	0.44
TRI	0.10	0.17	0.18

Q1 = 1×original flow rate, Q2 = 1.2 × original flow rate, Q3 = 1.4 × original flow rate

Table 5 Values of index WSSRegion for the numerical simulations (Pa)

Valve/flux	Q1	Q2	Q3
Bn1	1.27	1.65	2.30
Bn2	0.97	1.36	1.80
Bn3	0.74	1.15	1.31
TRI	0.46	0.58	0.72

Q1 = 1 × original flow rate, Q2 = 1.2 × original flow rate, Q3 = 1.4 × original flow rate

As expected WSS values were low in the tricuspid case and in the simulation with Bn3-Q1, which is the case with larger valve area and lower flow. When decreasing the valve area and increasing fluxes, the WSS values become higher up to 3 times the values obtained for the higher tricuspid case.

Finally, as shown in Fig. 7, the higher WSS values were found to be located for BAV cases in the typical location of aortic dilatation. Moreover, from this figure, we observe that the localized maximum WSS increases with the flow rate.

3.1.5 Helical flow pattern analysis

In Fig. 8, a top view of the PC-slice with the computed three-dimensional velocities in all the simulated cases is shown. It is evident from this figure the presence of a right-handed helical flow in BAV cases which is completely absent in TAV. At the bottom of each case, the quantity h is depicted in a color scale (red colors stand for $h > 0$, that is local right-handed helical structure, blue colors stand for $h < 0$, that is local left-handed helical structure and green colors stand

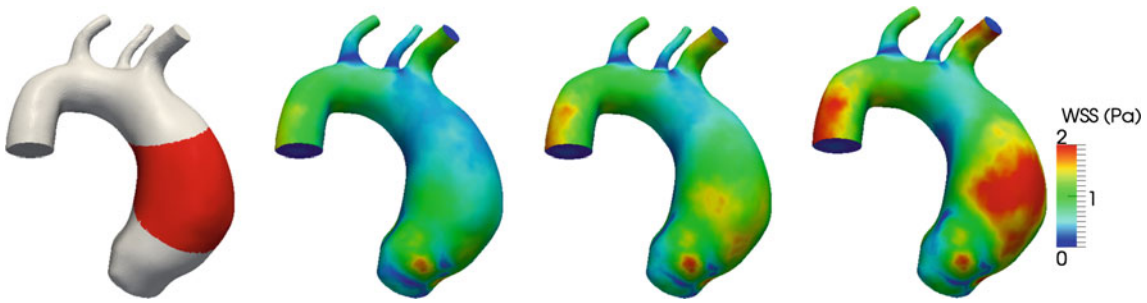

Fig. 7 From *left* to *right*: first, the aortic model with the area in which WSSRegion was measured (*red*). Next: WSS values for Bn1–Q1, Bn1–Q2 and Bn1–Q3. Q1 = 1 × original flow rate, Q2 = 1.2 × original flow rate, Q3 = 1.4 × original flow rate

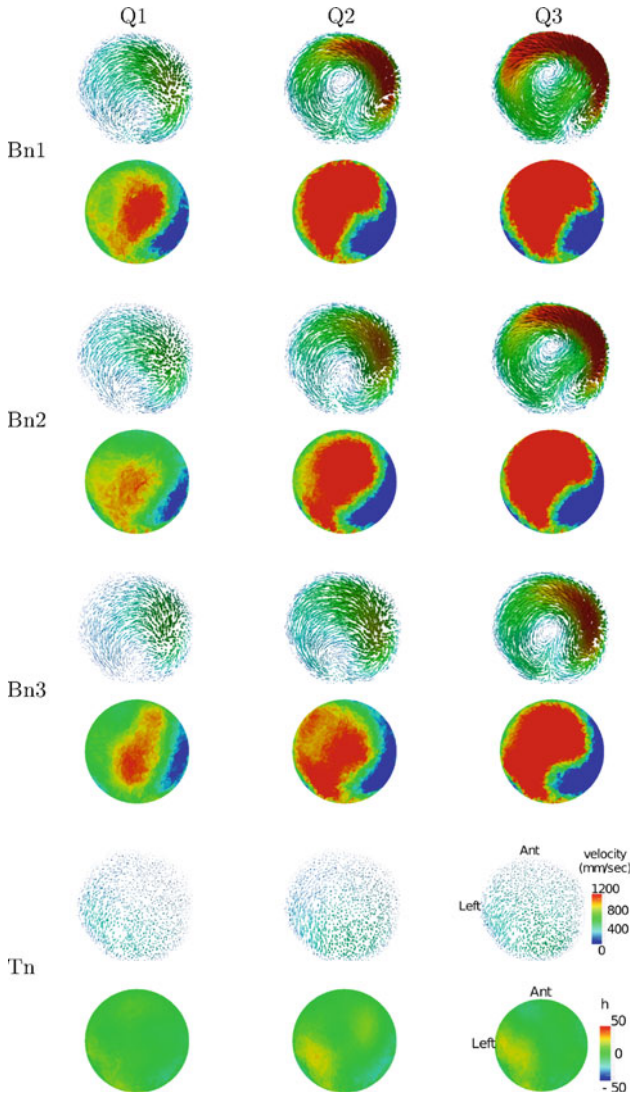

Fig. 8 Top view of the PC-slice with the computed three-dimensional velocity field and the corresponding h values for all the simulations (Q1 $=$ 1 $\times$ original flow rate, Q2 $=$ 1.2 $\times$ original flow rate, Q3 $=$ 1.4 $\times$ original flow rate). h *red colors* stand for $h > 0$, that is local right-handed helical structure, *blue colors* stand for $h < 0$, that is local left-handed helical structure and *green colors* stand for $h = 0$, that is no local helical structure

for $h = 0$, that is no local helical structure). In Table 6, we reported the values of index PHF for all the simulated cases. We observe that this index succeeded in describing the phenomenon highlighted by Fig. 8. Indeed, if we consider for example Bn1-Q3, the high prevalence of the right-handed rotation is captured (PHF $=$ 0.84), while Tn-Q3, for example, presented a less prevalence of one type of rotation over the other (PHF $=$ 0.62).

More in general, all BAV cases were characterized by a right-handed helical flow, which become more pronounced with smaller valve areas and higher flows (for BAV cases, PHF values range from 0.67 to 0.84). Moreover, even if TAV cases presented a slight prevalence of the right-handed rotation, we observe in Fig. 8 that TAV cases were characterized by an almost green distribution of h, indicating that the vortices are very small.

Table 6 Values of index PHF for numerical simulations

Valve/flux	Q1	Q2	Q3
Bn1	0.71	0.76	0.84
Bn2	0.70	0.76	0.79
Bn3	0.67	0.74	0.76
TRI	0.58	0.60	0.62

Q1 $=$ 1 $\times$ original flow rate, Q2 $=$ 1.2 $\times$ original flow rate, Q3 $=$ 1.4 $\times$ original flow rate

3.2 Data from biomedical images

The proposed indices calculated on clinical data are reported in Table 7.These data confirmed the presence of a retrograde flow, flow jet asymmetry and helical systolic flow in all BAV cases, being absent in the four TAV patients. Indeed, the average value of the three indices (see right column) was clearly larger in BAV patients. Despite the small number of subjects included in the study, in Table 7, we could recognize the same trends featured by our numerical simulations. Three of the four BAV patients had a similar A_{val}/A_{root} ratio (B1, B2 and B3, A_{val}/A_{root} equal to 0.26, 0.27 and 0.25, respectively). These three patients, as expected, presented similar values of FRR, NFA and PHF indices, except PHF value for B2 which is lower. A possible explanation is that this case featured a systolic flow rate of 7.9 l/min, considerably lower than those of the two other patients with similar valve orifices. B4 had a greater valve orifice ($A_{val}/A_{root} = 0.51$) and, as expected, presented values of the three indices lower than for the other patients. The trend highlighted by PHF is confirmed also by the visual inspection of the velocity field and of the quantity h reported in Fig. 9. In patients with small valve orifice (B1,B2 and B3), the red zone, representing right-handed helical flow, is more pronounced with respect to the blue (left-handed flow) and to the green (absence of helical flow) zones.

For what concerns TAV cases, Table 7 highlights that the values of all the three indices are considerably smaller than those featured by BAV patients, confirming the trend observed by numerical simulations. Figure 9 confirms the absence of a marked right-handed helical flow in these cases, featuring mainly blue and/or green zones.

4 Discussion

In recent years, considerable attention was devoted to the study of the "hemodynamic hypothesis". The first

Table 7 Systolic flow rate and ratio between the valve and root areas (top) and proposed indices (bottom) evaluated in BAV (B) and TAV (T)

Average values for BAV (Avg B) and TAV (Avg T) are also reported. X means data not available

	B1	B2	B3	B4	T1	T2	T3	T4	Avg B	Avg T
Q_{sys} (L/min)	13.63	7.93	21.60	6.51	21.38	24.35	31.86	32.35		
A_{val}/A_{root}	0.26	0.25	0.27	0.51	X	X	X	X		
FRR	46.72	55.77	49.66	43.78	0.98	3.59	1.81	0.20	48.98	1.65
NFA	0.59	0.61	0.61	0.23	0.01	0.06	0.07	0.02	0.51	0.04
PHF	0.82	0.55	0.83	0.55	0.22	0.23	0.16	0.06	0.69	0.24

characteristic fluid-dynamic phenomenon featured by BAV patients reported by several studies, both in-vivo and in-silico, consists in the presence of an eccentric flow jet in the ascending aorta (Barker et al. 2012; Della Corte et al. 2011; Den Reijer et al. 2010; Hope et al. 2010; Sigovan et al. 2011; Viscardi et al. 2010; Vergara et al. 2011). In Den Reijer et al. (2010), this asymmetry was found significantly correlated to the diameter at different levels of the ascending aorta, suggesting that the flow deflection is typically associated with ascending aorta dilatation. A second fluid-dynamic phenomenon reported so far consists in the observation that increased hemodynamic viscous forces placed on the proximal aorta could result in a possible progressive aortic dilatation (Della Corte et al. 2008). These two phenomena were linked together by the observation that the flow asymmetry was found to be strictly related to increased and localized wall shear stresses exerted on the dilated lumen surface, as highlighted in Barker et al. (2010, 2012); Hope et al. (2011); Viscardi et al. (2010); Vergara et al. (2011), and they were observed independently of the dilatation of the ascending aorta.

In recent years, a third fluid-dynamic phenomenon characterizing BAV patients was highlighted, an helical systolic flow in the ascending aorta in the presence of BAV (Hope et al. 2010; Barker et al. 2012), accompanied by the presence of a marked systolic retrograde flow (Barker et al. 2010). In this paper, we tried to elucidate the connections between flow asymmetry and high localized WSS, on the one hand, and helical flow and flow reversal, on the others, in BAV patients with a dilated ascending aorta. To this end, we studied the blood flow patterns in such cases by means of both numerical simulations and in-vivo data analysis with the rationale of using the findings from numerical simulations as a key for interpreting in-vivo phenomena. We performed a computational parametric study by varying, for a selected geometry, the valve area and the flow rate entering the aorta and, to perform comparisons, considering also a tricuspid case drawn in the same dilated aorta geometry. Finally, we considered in-vivo data obtained by PC-MRI sequences in four BAV and in four TAV cases.

To provide an objective quantification of the phenomena, we introduced a set of indices: the flow reversal ratio (FRR) to measure the presence of retrograde flow (Barker et al. 2010), the normalized flow asymmetry (NFA) index (Sigovan et al. 2011) to monitor the deflection of the systolic jet, WSS Region (Vergara et al. 2011) to quantify the systolic WSS and its localization, and the new positive helix fraction (PHF) index to quantify the degree of uniqueness of the helical flow. Except for WSSRegion which has been considered only for the numerical results, all the indices have been computed both for the numerical results and for the in-vivo imaging data.

Relation between single helical flow and asymmetric flows. BAV versus TAV. Both numerical and imaged-based results highlighted that BAV patients featured higher values of FRR, NFA and PHF indices when compared with those obtained in TAV configurations (see Tables 3, 4, 6, 7). Also, high WSS values were found to be strongly localized in BAV cases with respect to TAV, which features lower WSS for the highest flow rate also with respect to BAV cases with the lowest flow rate (see Table 5). This confirms the trend observed in Vergara et al. (2011) also for a dilated ascending aorta. This clearly confirmed that the fluid-dynamics in a dilated ascending aorta in the presence of BAV is markedly different from a TAV case featuring the same geometry. Indeed, the fluid-dynamics is characterized by high flow reversal, high flow asymmetry (see Fig. 6) and the presence of a right-handed vortex (see Figs. 8, 9). This is also clearly seen in Fig. 5, where the TAV case (on the right) did not feature any vortex and where the blood jet entered the aorta to reach the mid-ascending section by passing through the center of the vessel, leading to a nearly symmetric flow. Viceversa, in the BAV cases (see figures in the left and middle), a large right-handed vortex is observed, which fills up the central region of the vessel, forcing the blood jet to interplay the mid-ascending aorta by passing close to the aortic wall. This shows that in a dilated ascending aorta with normally functioning BAV, there is a clear correlation among the formation of a right-handed vortex, the presence of flow reversal and the deflection of the blood jet. This is in strong agreement with what was qualitatively observed through 4D PC-MRI images by Hope (Hope et al. 2010) who identified the presence of a systolic helical flow associated with eccentric systolic flow jet in 15 of 20 BAV patients but in none of normal or dilated TAV patients. We recall that our results were found for BAV patients without aortic coarctation or tetralogy of Fallot.

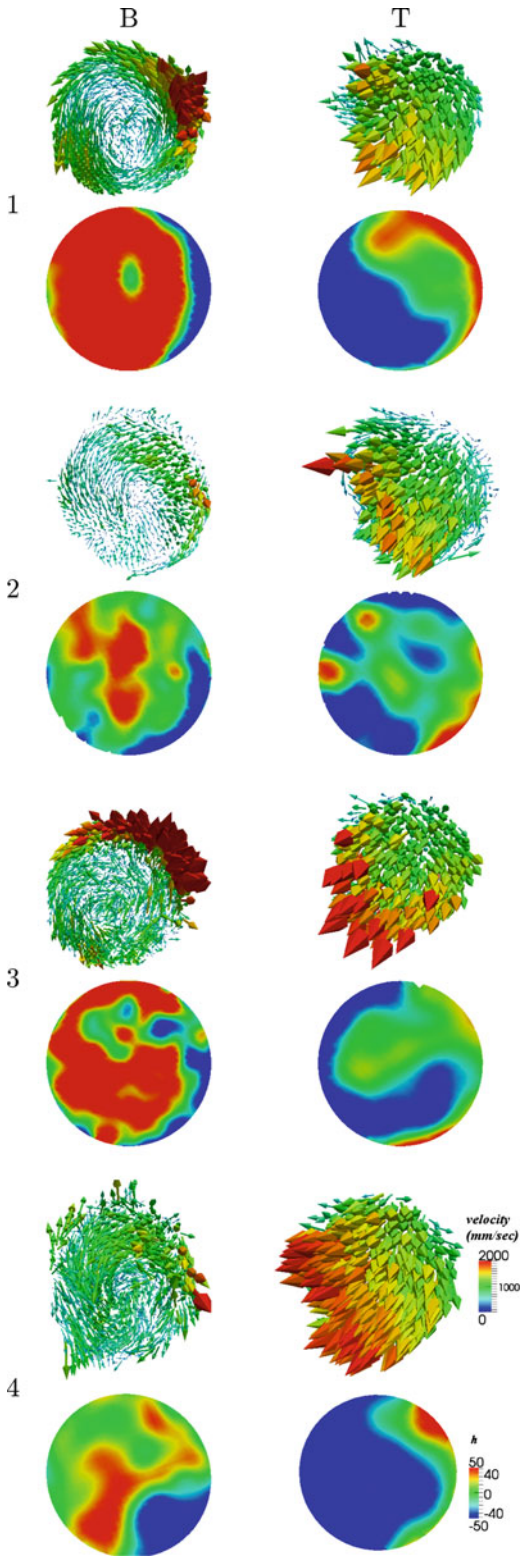

Fig. 9 Top view of the PC-slice with the measured three-dimensional velocity field and the corresponding h values for all the patients and controls. h *red colors* stand for $h > 0$, that is local right-handed helical structure, *blue colors* stand for $h < 0$, that is local left-handed helical structure and *green colors* stand for $h = 0$, that is no local helical structure

Observing the flow pattern in Fig. 5, we can hypothesize that the flow asymmetry induces the blood flow to fill up the central region of the vessel, leading to a single vortex. At the same time, it may be speculated that jet deflection toward the wall is exaggerated by the formation of a single vortex, since the flow maybe bumps on the pressure bubble created by the vortex, accentuating its asymmetry. Therefore, the two phenomena seem to be strongly interconnected and markedly related to BAV orifice morphology as evidenced by the results obtained when varying the valve area.

Relation between single helical flow and asymmetric flows. Varying flow rate and valve orifice area for BAV. By analyzing Tables 3, 4, 6 and 7, we observed that indices FRR, NFA and PHF featured a similar behavior both for the numerical results and for the in-vivo data. In particular, they both increased by decreasing the valve orifice area and/or by increasing the value of the flow rate. This further confirmed the strong connection between the formation of a right-handed helical flow and blood jet deflection. Again, this is confirmed by observing Fig. 5, left, where a large valve orifice area leads to a single vortex and asymmetry, that are less pronounced than in the case reported on the middle, featuring a smaller valve area.

Clinical implications. As observed, high and localized WSS in the ascending aorta are the effect of the blood jet deflection. For this reason, in Vergara et al. (2011), we proposed to use flow asymmetry (easily evaluated by imaging) as a surrogate of the localization of high WSS in the ascending aorta, and then as a simple indicator of the possible risk of dilatation. In Fig. 10 a plot showing the correlation between WSSRegion and NFA was reported to highlight the existing link between these two quantities. The Spearman correlation coefficient between WSSRegion and NFA was 0.9965 ($p < 4.2e-12$).In addition, due to the relation between flow asymmetry and the presence of a single vortex, we propose also the presence of a single vortex in a dilated ascending aorta as a surrogate marker of high localized WSS in the ascending aorta.

Agreement between numerical and in-vivo data. The results presented in this work showed a qualitative agreement between the pattern obtained with the numerical simulations and with those observed in the in-vivo analyses. This is clearly shown in Fig. 11 which plots the velocity vectors and the distribution of h at the PC-slice both for the computed and for the in-vivo solutions. In particular, we observe a good qualitative agreement between the two reported cases.

This is an important point for future analyses, since it highlights the reliability of computational tools for such investigations.

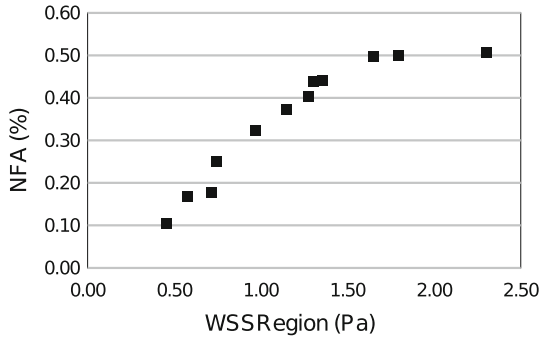

Fig. 10 Correlation between WSSRegion and NFA

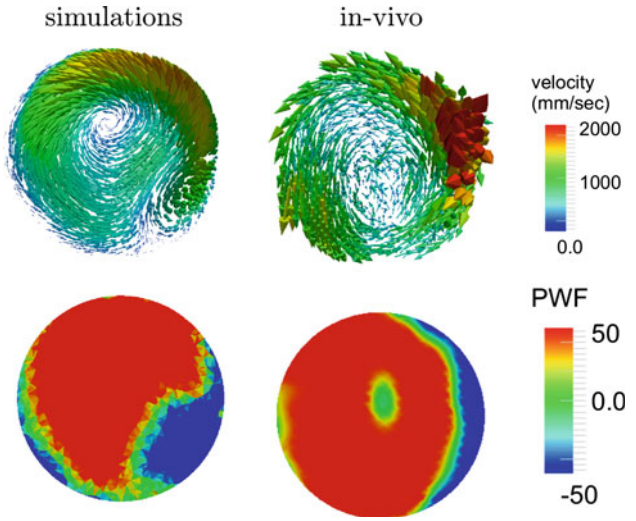

Fig. 11 Velocity field (*top row*) and h distribution (*bottom row*) obtained from the numerical simulation (*left*) and from in-vivo data (*right*). For the numerical simulation, we considered case Bn1 with flow rate Q3, while for the in-vivo data, we considered patient B1

Additionally, it is important to point out that the deflection of the jet is recovered in our simulations without modeling the leaflets, obtaining values of NFA comparable to those extracted by in-vivo data. This seems to imply that the particular shape of the orifice in BAV cases possibly combined with the shape of the ascending aorta (not necessarily, or in addition to, the presence of the leaflets, as suggested in Barker et al. 2012 and Della Corte et al. 2011) are the primary cause in the generation of the flow deflection.

Limitations. Limitations of our study rely on the availability of few in-vivo data. A more comprehensive study is mandatory to better understand our first highlighted results.

The main model limitation of this work concerns some of the hypotheses introduced for the numerical simulations. First of all, the assumption of rigid walls is probably simplistic, since the motion of the aorta (due both to the interaction with blood and to the rigid movement of the heart) is not negligible. However, we argued that, owning to the good agreement between imaging and simulation data, the modeling strategy we adopted is adequate for the scope of the present work.

Another simplification adopted in our simulations is that the issue of turbulence was not explicitly addressed by adopting a turbulence model. While in healthy subjects, the blood flow is usually laminar and does not experience transition to turbulence (Nichols and O'Rourke 1998), it is possible that a bicuspid valve leads to transitional flows. Despite this consideration, finding an adequate model of turbulence for aortic flow is a currently open problem. For this reason, we preferred to avoid adopting a turbulence model, and instead, we carefully resolved the mesh in order to capture the phenomena of interest. The agreement between flow patterns in-vivo and those resulting from our simulations seems to suggest that our choice was appropriate for the purposes of the present work.

Moreover, we did not take into account the mechanisms of valve opening and closing nor the longitudinal influence of the leaflets. In fact, all of our numerical simulations were performed with an open valve configuration without the presence of the leaflets. As previously discussed, this is not a true limitation since our results highlighted that the flow asymmetry is generated without modeling the leaflets.

Moreover, in the model used for all numerical simulations, the Valsalva sinuses were neglected (see Fig. 2) because not visible in the CE-MRI image used to construct the model. While the sinuses are potentially relevant for aortic root hemodynamics during the cardiac cycle, our results seem to show that their effect in determining jet deviation during systolic ejection is minor.

At last, in order to do a parametric study, we have maintained fixed shape of the flow waveform. This is a simplification since this changes with patients and in particular with $A_{\mathrm{val}}/A_{\mathrm{root}}$: in general, higher values of the ratio lead to an earlier peak of the flow rate during systole.

Acknowledgments This work has been (partially) supported by the ERC Advanced Grant N. 227058 MATHCARD and by the Italian MIUR PRIN09 project n. 2009Y4RC3B_001. The numerical simulations have been performed at CILEA Consortium through a LISA Initiative (Laboratory for Interdisciplinary Advanced Simulation) 2012 grant (link: http://lisa.cilea.it).

Appendix: Grid convergence analysis

Three finite element meshes of progressively greater refinement were generated consisting of 0.9×10^6, 1.36×10^6 and 1.8×10^6 tetrahedra, respectively. For grid convergence, the four indices introduced to describe the fluid-dynamics in the ascending aorta were used (i.e., FRR, NFA, WSSRegion and PHF). Richardson's extrapolation was used to find extrapolated values, and grid convergence analysis was performed

Table 8 Grid convergence study results

	FRR	NFA	WSSRegion	PHF
N_1, N_2, N_3	1800399, 136550, 921245			
r_{21}	1.32			
r_{32}	1.48			
Φ_1	9.31	0.32	1.00	0.67
Φ_2	9.20	0.32	0.97	0.68
Φ_3	10.77	0.40	0.78	0.64
p	6.91	5.51	4.28	6.48
Φ_{ext}^{21}	9.33	0.31	1.01	0.67
e_a^{21}	1.2 %	2.31 %	3 %	0.54 %
e_{ext}^{21}	0.21 %	0.65 %	1.31 %	0.11 %
$\text{GCI}_{\text{fine}}^{21}$	0.26 %	0.81 %	1.65 %	0.13 %

according to Celik et al. (2008). The results were reported in Table 8: for each index, N is the number of elements, r the refinement ratios, the term Φ_i gives the results of the index computed with the mesh i, p is the apparent rate of convergence, Φ_{ext}^{21} is the extrapolated value, e_a^{21} is the apparent error, e_{ext}^{21} the extrapolated error and $\text{GCI}_{\text{fine}}^{21}$ is the grid convergence index (Celik et al. 2008). On the ground of these results, the $N = 1.36 \times 10^6$ mesh was used for all further simulations.

References

Antiga L, Piccinelli M, Botti L, Ene-Iordache B, Remuzzi A, Steinman D (2008) An image-based modeling framework for patient-specific computational hemodynamics. Med Biol Eng Comput 46:1097–1112

Baltes C, Hansen M, Tsao J, Kozerke S, Rezavi R, Pedersen E, Boesiger P (2008) Determination of peak velocity in stenotic areas: echocardiography versus kt sense accelerated mr fourier velocity encoding1. Radiology 246(1):249–257

Barker A, Markl M (2011) Editorial: the role of hemodynamics in bicuspid aortic valve disease. Eur J Cardio-thorac Surg 39(6): 805–806. doi:10.1016/j.ejcts.2011.01.006

Barker A, Lanning C, Shandas R (2010) Quantification of hemodynamic wall shear stress in patients with bicuspid aortic valve using phase-contrast mri. Ann Biomed Eng 38(3): 788–800. doi:10.1007/s10439-009-9854-3

Barker AJ, Markl M, Bürk J, Lorenz R, Bock J, Bauer S, Schulz-Menger J, von Knobelsdorff-Brenkenhoff F (2012) Bicuspid aortic valve is associated with altered wall shear stress in the ascending aorta. Clinical perspective. Circ Cardiovasc Imaging 5(4):457–466

Bauer M, Siniawski H, Pasic M, Schaumann B, Hetzer R (2006) Different hemodynamic stress of the ascending aorta wall in patients with bicuspid and tricuspid aortic valve. J Cardiac Surg 21(3): 218–220

Beroukhim RS, Kruzick TL, Taylor AL, Gao D, Yetman AT (2006) Progression of aortic dilation in children with a functionally normal bicuspid aortic valve. Am J Cardiol 98(6):828–830

Chandra S, Rajamannan N, Sucosky P (2012) Computational assessment of bicuspid aortic valve wall-shear stress: implications for calcific aortic valve disease. Biomech Modeling Mechanobiol. doi:10.1007/s10237-012-0375-x

Celik IB, Ghia U, Roache PJ, Freitas CJ, Coleman H, Raad PE (2008) Procedure for estimation and reporting of uncertainty due to discretization in CFD applications. J Fluids Eng Trans ASME 130: 078001-1–078001-4. doi:10.1115/1.2960953

Della Corte A, Quarto C, Bancone C, Castaldo C, Di Meglio F, Nurzynska D, De Santo L, De Feo M, Scardone M, Montagnani S et al (2008) Spatiotemporal patterns of smooth muscle cell changes in ascending aortic dilatation with bicuspid and tricuspid aortic valve stenosis: focus on cell-matrix signaling. J Thorac Cardiovasc Surg 135(1): 8–18. doi:10.1016/j.jtcvs.2007.09.009

Della Corte A, Bancone C, Conti C, Votta E, Redaelli A, Del Viscovo L, Cotrufo M (2011) Restricted cusp motion in right-left type of bicuspid aortic valves: a new risk marker for aortopathy. J Thorac Cardiovasc Surg. doi:10.1016/j.bbr.2011.03.031

Den Reijer P, Sallee D III, Van Der Velden P, Zaaijer E, Parks W, Ramamurthy S, Robbie T, Donati G, Lamphier C, Beekman R et al (2010) Hemodynamic predictors of aortic dilatation in bicuspid aortic valve by velocity-encoded cardiovascular magnetic resonance. J Cardiovasc Magn Reson 12(4). doi:10.1186/1532-429X-12-4

Formaggia L, Quarteroni A, Veneziani A (eds) (2009) Cardiovascular mathematics: modeling and simulation of the circulatory system, modeling, simulation and applications, vol 1. Springer, Milan

Fowles R, Martin R, Abrams J, Schapira J, French J, Popp R (1979) Two-dimensional echocardiographic features of bicuspid aortic valve. Chest 75(4):434–440

Girdauskas E, Borger M, Secknus M, Girdauskas G, Kuntze T (2011) Is aortopathy in bicuspid aortic valve disease a congenital defect or a result of abnormal hemodynamics? A critical reappraisal of a one-sided argument. Eur J Cardio-thorac Surg 39(6):809–814

Hahn R, Roman M, Mogtadek A, Devereux R (1992) Association of aortic dilation with regurgitant, stenotic and functionally normal bicuspid aortic valves. J Am Coll Cardiol 19(2):283–288

Haycock G, Schwartz G, Wisotsky D (1978) Geometric method for measuring body surface area: a height-weight formula validated in infants, children, and adults. J Pediatr 93(1):62–66

Hope T, Markl M, Wigström L, Alley M, Miller D, Herfkens R (2007) Comparison of flow patterns in ascending aortic aneurysms and volunteers using four-dimensional magnetic resonance velocity mapping. J Magn Reson Imaging 26(6): 1471–1479. doi:10.1002/jmri.21082

Hope M, Hope T, Meadows A, Ordovas K, Urbania T, Alley M, Higgins C (2010) Bicuspid aortic valve: four-dimensional mr evaluation of ascending aortic systolic flow patterns1. Radiology 255(1): 53–61. doi:10.1148/radiol.09091437

Hope M, Hope T, Crook S, Ordovas K, Urbania T, Alley M, Higgins C (2011) 4d flow cmr in assessment of valve-related ascending aortic disease. JACC Cardiovasc Imaging 4(7):781–787

Moireau P, Xiao N, Astorino M, Figueroa CA, Chapelle D, Taylor CA, Gerbeau JF (2012) External tissue support and fluidstructure simulation in blood flows. Biomech Modeling Mechanobiol 11 (1–2):1–18

Morbiducci U, Gallo D, Ponzini R, Massai D, Antiga L, Montevecchi FM, Redaelli A (2010) Quantitative analysis of bulk flow in image-based hemodynamic models of the carotid bifurcation: the influence of outflow conditions as test case. Ann Biomed Eng 38(12):3688–3705

Nichols W, O'Rourke M (1998) Mcdonalds blood flow in arteries: theoretical, experimental and clinical principles. Edward Arnold, London

Nkomo V, Enriquez-Sarano M, Ammash N, Melton L, Bailey K, Desjardins V, Horn R, Tajik A (2003) Bicuspid aortic valve asso-

ciated with aortic dilatation. Arteriosclerosis Thromb Vasc Biol 23(2):351–356

Roman M, Devereux R, Kramer-Fox R, O'Loughlin J (1989) Two-dimensional echocardiographic aortic root dimensions in normal children and adults. Am J Cardiol 64(8):507–512

Sievers HH, Sievers HL (2011) Aortopathy in bicuspid aortic valve diseasegenes or hemodynamics? or Scylla and Charybdis?. Eur J Cardio-thorac Surg 39(6):803–804

Sigovan M, Hope M, Dyverfeldt P, Saloner D (2011) Comparison of four-dimensional flow parameters for quantification of flow eccentricity in the ascending aorta. J Magn Reson Imaging 34:1226–1230

Vergara C, Viscardi F, Antiga L, Luciani GB (2011) Influence of bicuspid valve geometry on ascending aortic fluid dynamics: a parametric study. Artif Organs 36(4):368–378

Viscardi F, Vergara C, Antiga L, Merelli S, Veneziani A, Puppini G, Faggian G, Mazzucco A, Luciani GB (2010) Comparative finite element model analysis of ascending aortic flow in bicuspid and tricuspid aortic valve. Artif Organs 34(12):1114–1120